Contents lists available at ScienceDirect

Composites Part A

journal homepage: www.elsevier.com/locate/compositesa

Experimental study on nonlinearity of unidirectional carbon fibre-reinforced shape memory polymer composites

Dou Zhang [a], Liwu Liu [a], Xin Lan [b], Fengfeng Li [a], Yanju Liu [a,*], Jinsong Leng [b,*]

[a] *Department of Astronautical Science and Mechanics, Harbin Institute of Technology, Harbin 150001, People's Republic of China*
[b] *Centre for Composite Materials and Structures, Harbin Institute of Technology, Harbin 150080, People's Republic of China*

ARTICLE INFO

ABSTRACT

A comprehensive and detailed experimental study has been conducted on shape memory polymer composites (SMPCs) with different reinforcements, thicknesses, fibre volume fractions and distributions. Monotonic test results show temperature-dependent mechanical properties. Cyclic loading–unloading tests, including constant and incremental strain-controlled tests, were conducted in three-point bending and transverse tension to investigate softening and reusable characteristics. The fibre postbuckling behaviour for samples undergoing bending deformation combines geometrical and material nonlinearities. While for transverse tension, all possible sources of nonlinearity are due to the material responses. The energy properties were highly fibre volume fraction- and strain amplitude-dependent. The stiffness was also sensitive to the degree of fibre clustering. The focus of this work is not on the examination of basic elastic constants, but on the nonlinear and reusable responses of SMPCs, which can be used for both the design of aerospace deployable mechanisms and analyses of the damage process.

1. Introduction

Shape memory polymers (SMPs) are typical smart materials which can maintain a temporary shape and recover their initial configuration under certain external stimuli as shown in Fig. 1 [1–3]. Carbon fibre-reinforced plastics (CFRPs) are gaining more and more attention in engineering communities primarily because they have the advantages of high strength and low weight [4]. Carbon fibre-reinforced shape memory polymer composites (SMPCs) offer a synergetic combination of mechanical enhancement and shape memory effect [5]. The temperature-dependent stiffness [6] and fibre post microbuckling behaviour [7] provide SMPCs with a highly nonlinear mechanical response, which is essential for deployable structures. Therefore, their applications have spread into many areas, especially in aerospace [8]. They have been verified suitable by orbital qualifications in 2016 as a sunlight-stimulated substrate [9], and in 2019 in the form of a flexible solar array system [10]. Compared with traditional composites, the design of SMPCs is more complex because the mechanical issues and deformable aspects related to the shape memory behaviour must be taken into account simultaneously.

Solid progress has been made in theoretical models regarding the

mechanisms of SMPs, including three categories: viscoelastic rheological methods [11,12], mesomechanical phase transition theory [13,14] and models combining these two [15–18]. SMPs become soft when the temperature is higher than its glass transition temperature (Tg), and the slender but stiff fibres in Fig. 1 buckle when the composite undergoes compression. This microbuckling is regarded as a failure mode for regular CFRPs, however, for SMPCs, the fibre microbuckling is a stress relief mechanism that allows the material to deform far beyond the critical elongation of fibres. Consequently, the prediction of fibre microbuckling behaviour plays a key role in the design of deployable structures based on SMPCs. Aiming at the constitutive behaviour of the reinforcement and matrix under the limited deformation, theoretical methods include homogenisation theory [19], Bloch Wave theory [20] and strain energy function method [7,21]. Among them, the strain energy method is widely used. The total strain energy includes the tensile, compressive, and shear strain energies of each phase and the shear strain energy of the interaction between phases. The deformation behaviour can be solved by the minimum energy principle and variational approach.

In terms of experimental studies, the existing literature could be grouped into two categories: thermo-mechanical behaviour of SMPs [22–24] and mechanisms of the unidirectional (UD) fibre-reinforced

---

SMPCs undergoing bending deformation [7,25]. However, these works focused on the microbuckling architectures of fibres and neglected the mechanical response of laminae. UD carbon fibre-reinforced SMPCs with different fibre mass fractions were tested by a series of three-point bending tests [26], which were representative of deformation form in most of SMPCs' applications. However, SMPs are viscoelastic and strongly nonlinear. The bending deformation combined the geometrical and material nonlinearities. Therefore, although this work has given a comprehensive understanding of the constitutive modelling of the material, the results are, however, inadequate to analyse the material's nonlinearity and reusability. In addition, apart from the fibre content, other design parameters such as the reinforcement, lamina thickness, and fibre distribution still need to be investigated. The final topic is the Mullins effect, well-known in particle-reinforced rubbers [27]. The SMP acts as rubber in its deformable temperatures. The stress softening occurs on each successive loading–unloading cycle. The reduction of stress is greatest during the reloading after the virgin loading and converges to a certain value subsequently, which plays an important role in mechanical response of deployable structures during repeated usage. This phenomenon is thought to increase with the filler content [28]. Several physical interpretations have been proposed to explain this effect, including chain breakage at the filler-matrix interface, rupture of fillers, chain entanglement and crystallization. The Mullins effect is manifested as a hysteresis loop in stress–strain curves, which represents the energy dissipation property [29,30].

The elastic constants in UD carbon fibre-reinforced SMPCs have been predicted by the phase transition model and validated by experimental results [31]. However, under the combined influence of temperature and loading, the deformation of the fibres and matrix does not match. Therefore, although there exist many studies relating to the mechanics of UD lamina, the deformation of the SMPC has not been thoroughly studied yet. Therefore, in this paper, from the perspective of engineering applications, we focus on the nonlinear and reusable response of these composites. The fibre microbuckling behaviour is affected by the bending curvature, modulus ratio of the fibre and matrix, lamina thickness and the fibre volume fraction [7]. Besides, the fibre distribution pattern also plays a significant role, with functionally graded plates [21] and randomly distributed models [28] studied. Therefore, a series of UD carbon fibre-reinforced epoxy-based SMPCs with different reinforcements, thicknesses, fibre volume fractions and distributed patterns have been fabricated and characterised. Experiments were conducted in the form of monotonic and cyclic loading–unloading tests. As for monotonic tests, longitudinal tensions, three-point bending tests, and transverse tensions were all carried out for a comprehensive understanding of the temperature-dependent properties. For cyclic loading–unloading tests, only the three-point bending and transverse tension were considered to analyse their nonlinear responses and reusable characteristics.

2. Experimental

2.1. Material preparation and characterisation

The SMPCs are composed of matrix and fibres, where the matrix exhibits the shape memory effect and fibres enhance the mechanical properties. The matrix used is an epoxy-based SMP produced by Jinsong Leng's group, which consists of an epoxy resin, a hardener and a linear monomer [32]. The T_g is obtained from a dynamic mechanical analysis (DMA) analyser (NETZSCH Instruments, Germany) with a tension mode at a heating rate of 3 °C/min from 25 °C to 160 °C and a frequency of 1 Hz. The storage modulus and tan delta are depicted in Fig. 2 (a). Tan delta is the ratio of the dynamic loss modulus to storage modulus, and the temperature corresponding to the peak value of this curve represents the T_g, which is about 94 °C. The storage modulus experiences three regions: the glassy state, glass transition region and rubbery state, exhibiting an approximately 100 times decrease. This temperature-dependent characteristic can also be investigated by isothermal tensile tests. The specimens were prepared by a laser cutting machine according to ASTM D638 type IV and tested by a Zwick Roell 010 universal testing machine with a 1 kN load cell. The specimens were heated in a thermal chamber at six target temperatures: 25 °C (room temperature), 40 °C, 60 °C, 80 °C, 100 °C and 120 °C for twenty minutes, and then tested at a loading rate of 2 mm/min until broke. The tensile stress in Fig. 2 (b) demonstrates a sharp decrease from 60 °C, agreeing with the DMA results. The SMP demonstrates significant temperature-dependent stiffness, with its tensile modulus decreases from 1.1 GPa at room temperature to 7 MPa around T_g.

Fibres used are Toray's Torayca yarns T300B-1K, T300B-3K and T400HB-6K to fabricate laminae with various thicknesses, fibre volume fractions and distributions. The physical properties of these reinforcements are listed in Table 1 [33]. Differences in tensile modulus, strength, and elongation are observed between T300B and T400HB, while they are within 9 %, and these two bundles can be used for a preliminary study.

Fibre postbuckling behaviour is the key design basis for the UD lamina studied here. The microbuckling mechanics of fibre-reinforced SMPCs has been investigated by Lan et. al [7]. As shown in Fig. 3 (a-b), fibres will buckle in sinusoidal shape when lamina subjected to compression exceeding the critical buckling load. It can be seen in Fig. 3 (c) that fibres in composites undergoing bending deformation are in three states: compression & buckling state, compression & non buckling state, tension & non-buckling state. The cross section in Fig. 3 (d) is divided into three zones by introducing the critical buckling surface z_{cb}, and neutral surface z_{ns}, correspondingly. Expressions of key parameters have been obtained through self-consistent approach according to the minimum energy principle. The half-wavelength and amplitude of buckled fibres, and the critical buckling surface are strongly dependent on the fibre volume fraction and lamina thickness. Furthermore, the fibre distribution pattern has been pointed out as another factor affecting macroscopic bending deformation of SMPCs and microscopic buckling behaviour of fibres [21,28].

The modified manual winding method is inspired by the conventional filament winding technique, of which the fabrication details have been illustrated in our previous work [34]. The serrated rotating plate in Fig. 4 (a) guaranteed uniform and precise winding. The aligned dry carbon fibre assemblies were placed into a curing mould made of two glass plates affixed with Teflon cloth and sealed by a silicone strip that controlled the thickness in Fig. 4 (b). Fibres were held in tension during resin infusion in Fig. 4 (c) and curing process in Fig. 4 (d) to prevent process-induced waviness. Composites were cured at three steps: 80 °C for 3 h, 100 °C for 3 h and 150 °C for 5 h. The fibres in de-moulded lamina in Fig. 4 (e) were highly aligned and uniformly distributed,
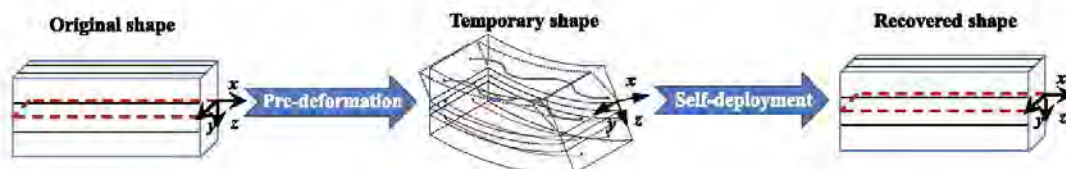

Fig. 1. Schematic diagram of shape memory effect with fibre post microbucking behaviour.
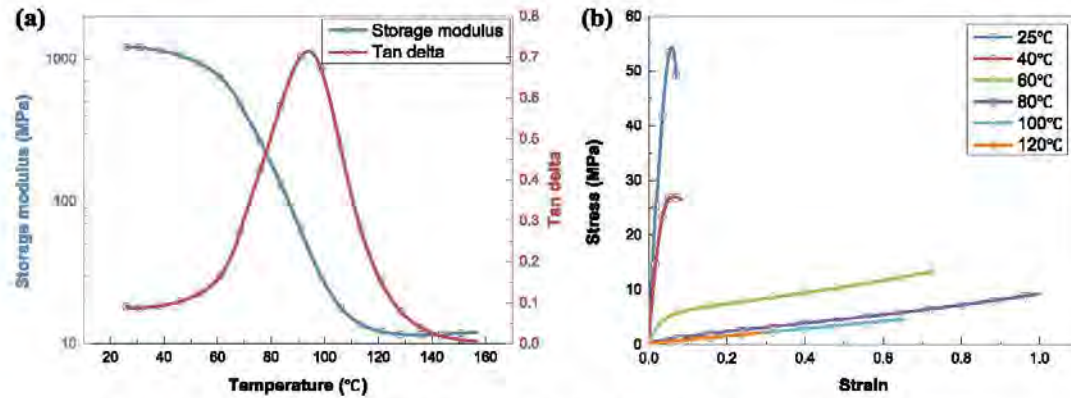
Fig. 2. Mechanical properties of the epoxy-based SMP, (a) DMA results and (b) tensile results at different temperatures.

Table 1
Physical properties of carbon fibre reinforcements [33].

Product No.	Filament	Fibre diameter (μm)	Tensile modulus (GPa)	Elongation (%)	Tensile strength (MPa)
T300B-1K	1000	7	230	1.5	3530
T300B-3K	3000				
T400HB-6K	6000	7	250	1.8	4410

although initial fibre misalignments were more common in plates reinforced by thicker fibre bundles such as 3 k yarns in Fig. 4 (e2) and 6 k yarns in Fig. 4 (e3). Finally, samples in required dimensions were obtained by a computer-numerical-controlled (CNC) engraving and milling machine in Fig. 4 (f).

Synthesis the above theoretical analysis and fabrication technique, fibre volume fraction, lamina thickness and fibre distribution are three factors in design of SMPCs. The carbon fibre assembly in Fig. 4 (a) produced by a single winding operation contains two carbon fibre layers. These two fibre layers are separated by the rotating plate, while the thickness of adjacent layers in different assemblies in Fig. 4 (b) is

controlled by filler strips. Fibre content in a single layer is governed by different bundles (1 k, 3 k and 6 k) wound on the same rotating plate. The overall lamina thickness is controlled by the seal strip in Fig. 4 (b). For SMPCs with a fibre volume fraction of 20 % and a thickness of 2 mm, fibre fracture has been observed when bending curvature is 100 m^{-1} [7]. Given that one of the greatest advantages of SMPCs over pyroshock [35] is reusability, and high deploy-to-package ratio is desired, three lamina thicknesses of 2 mm, 3 mm and 4 mm are designed. The fibre volume fraction is governed by the bundle type, number of layers and the lamina thickness, and in this work, it is designed to be 4.32 %, 6.48 % and 12.96 % to achieve recoverable bending deformation. The fibre distribution can also be investigated by those samples with the same lamina thickness and fibre volume fraction, but different bundle types and numbers of layers. Therefore, six sets of laminae have been designed and labelled by three parameters: the first is the number of fibres in a strand; the second is the number of fibre layers; the last denotes the lamina thickness in millimetres. The prepared samples in Fig. 5 (a) reveal very high-quality laminae with evenly fibre distribution and no visible porosity, while some processing-induced defects are captured by an optical microscope in Fig. 5 (b). The misalignments in Fig. 5 (b1) and (b2) are 1.42° and 6.61°, respectively, which are observed on a few fibres. Apart from misalignments, the waviness localized in resin rich areas in Fig. 5 (b3) is seen because the fibre volume fractions are much lower than
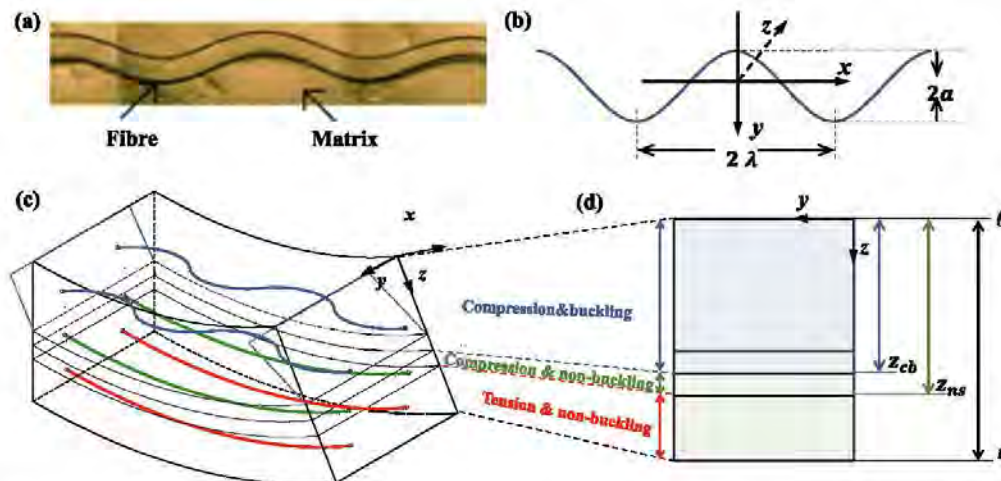

Fig. 3. Fibre microbukling behaviour, (a) SMPCs under compression load [7], (b) sinusoidal shape of buckled fibres, (c) schematic diagram of the SMPC undergoing bending deformation, (d) zones in cross section.
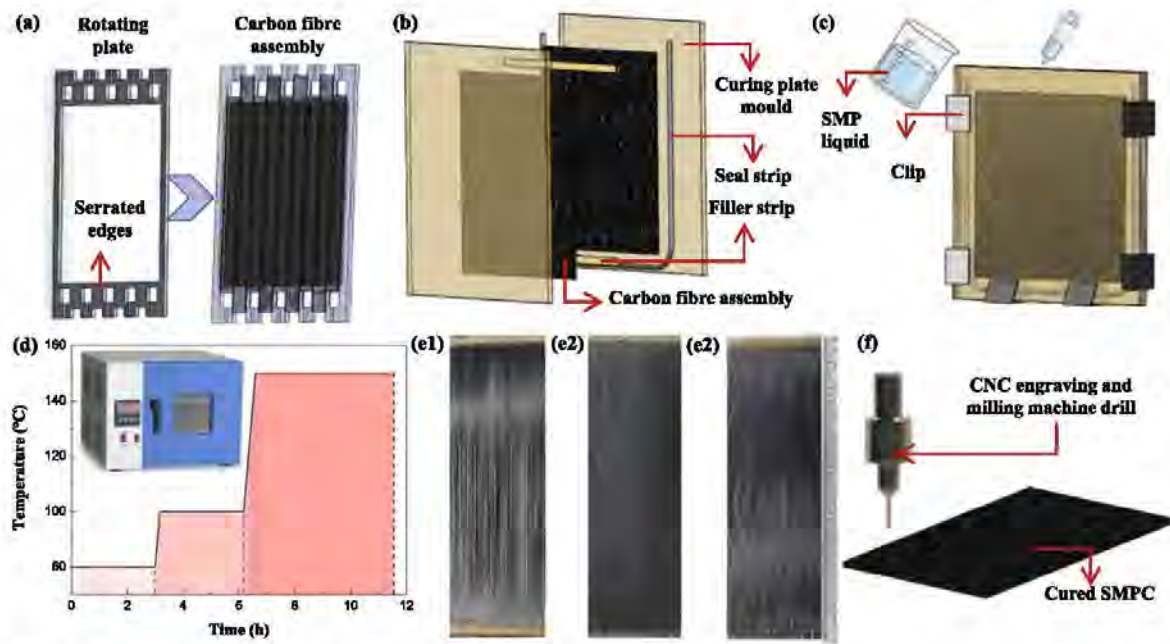
Fig. 4. Material preparation, (a) manual filament winding method, (b) curing mould, (c) polymer infusion method, (d) three-step curing process, (e) cured plate with (e1) 1 k, (e2) 3 k and (e3) 6 k bundles, (f) material cutting method.

regular CFRPs. However, different from the rigid matrix composites where initial imperfections have been identified to progress into failure sites under loading [36], the fibre microbuckling has been confirmed to be a bifurcation phenomenon rather than a collapse of the existing waviness [37].

The spatial distribution of fibres heavily depends on the fabrication technique. The characterisation of the fibre distribution, impregnation quality of fibre bundles and the fibre matrix interaction is the prerequisite for the mechanical analysis. At least three samples dimensioned in 10 mm in width, 10 mm in length and the whole thickness for each set of laminae were cut randomly from plates and embedded in an epoxy matrix holder. The cross-sections of these samples were then polished using grids of 600, 1200, 2500 and 4000, and the 6 μm monocrystalline diamond suspension. An optical microscope (Nikon digital camera D5200) was used to observe and capture microscopy images. The cross-section of 1k-4l-t2 lamina is shown in Fig. 5 (c) with pores highlighted in red, and in Fig. 5 (d) throughout the thickness. The epoxy wets the fibres at the pre-polymer stage and the sample shows good fibre impregnation.

The measured thickness in Fig. 6 are 1.78 mm (1k-4l-t2), 1.82 mm (3k-2l-t2), 3.71 mm (3k-4l-t4), 2.75 mm (3k-4l-t3), 1.78 mm (3k-4l-t2) and 1.73 mm (6k-2l-t2). These results are 7.5 % to 13.75 % lower than the designed ones because the silicon strips were compressed. The fibre and porosity volume fractions were calculated by ratios of the fibre and porosity areas to the cross-section area, respectively. The averaged fibre volume fraction shown in Fig. 6 are 4.32 % for 1k-4l-t2, 6.36 % for 3k-2l-t2, 6.24 % for 3k-4l-t4, 8.42 % for 3k-4l-t3, 12.97 % for 3k-4l-t2 and 13.40 % for 6k-2l-t2, showing inevitable but slight differences from the designed ones. The porosity volume fraction varies from 0.05 % to 0.2 % and shows a slight increase in thick fibre bundles. This is reasonable because the thicker bundles result in more significant fibre concentrations. The errors of the thickness, fibre volume fraction and porosity volume fraction are all less than 10 %, which implies a good consistency of the material.

These samples are categorized into four groups. First, 1k-4l-t2 & 3k-2l-t2 & 3k-4l-t2, these three types of laminae have the same reinforcement (T300B carbon fibres), lamina thickness, and therefore, can be used to study the influence of fibre volume fraction. Second, 3k-2l-t2 & 3k-4l-t4, these laminae possess the same fibre bundles and fibre volume fraction. The effect of the lamina thickness can be analysed. Third, 3k-4l-t2 & 6k-2l-t2 are designed to have the same fibre volume fraction and thickness. The distribution of filaments can be investigated, despite the limited differences in their mechanical properties. Finally, for 3k-4l-t4 & 3k-4l-t3 & 3k-4l-t2, although they have different fibre volume fractions and lamina thicknesses, the reinforcement and the number of fibre layers are the same.

2.2. Monotonic mechanical tests

To facilitate the applications of these materials in critical components, monotonic mechanical tests were carried out at six target temperatures (25 °C, 40 °C, 60 °C, 80 °C, 100 °C and 120 °C) which were guaranteed by a thermal chamber. The Shimadzu AGS-X with a 150 kN load cell was used for longitudinal tensions, and the Zwick Roell 010 with a 1 kN load cell was chosen for three-point bending and transverse tension tests. Tensions were carried out for the temperature-dependent mechanical properties. Three-point bending tests were conducted to obtain the flexural response since deployable structures usually underwent bending deformation. Specimens were first heated to target temperatures at a heating rate of 3 °C/min and then left at that temperature for 20 min to achieve internal thermal uniformity. These tests were first preloaded at 2 N with a crosshead velocity of 1 mm/min, and controlled by displacement loading until the specimens reached the maximum strain or broke before that.

2.2.1. Tension along the fibres

Longitudinal tension tests were conducted at 2 mm/min with specimens cut according to ASTM D3039 [38] in a dimension of $250mm \times 15mm$. As shown in Fig. 7 (a), strains along the fibres and transverse to the fibres were monitored by two strain gauges and recorded by a Donghua DH5981 dynamic signal acquisition system. Then the Poisson's
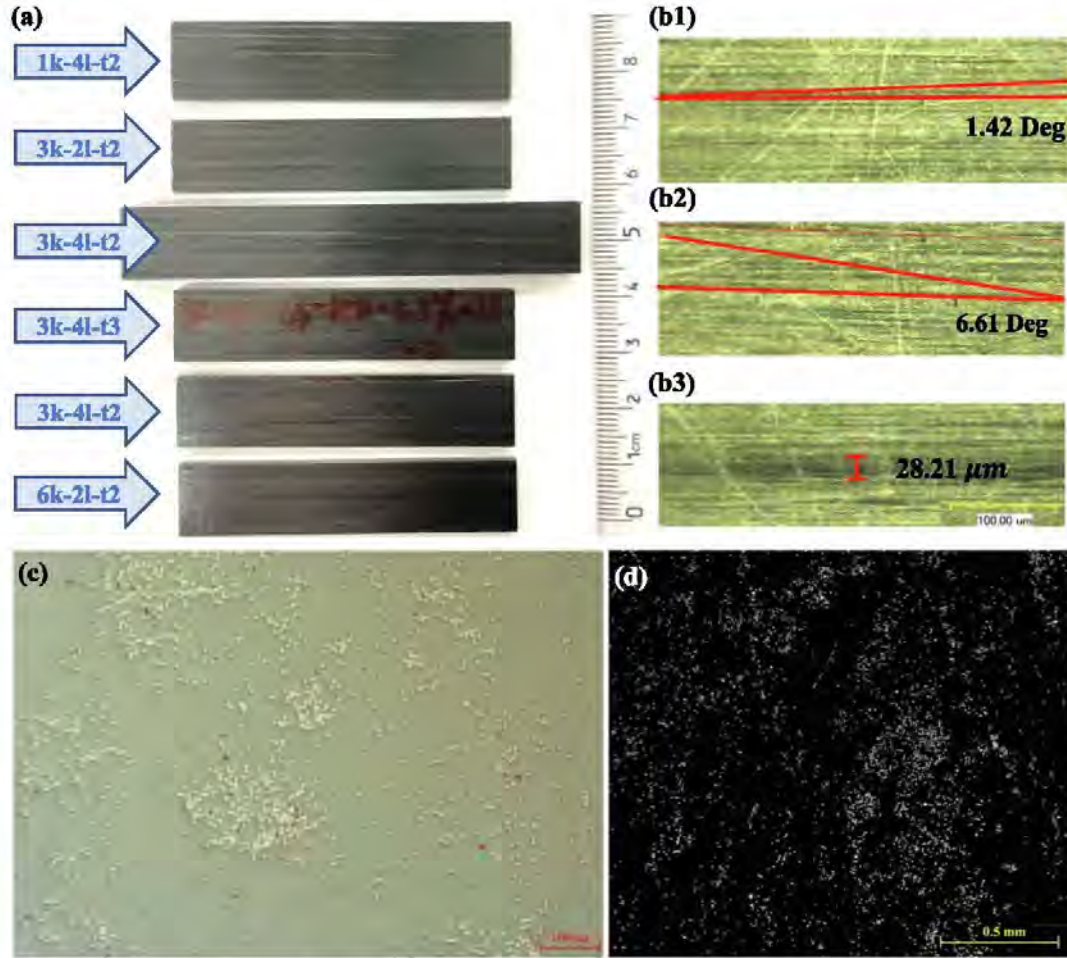
Fig. 5. The fabricated samples, (a) macroscopic images of the six sets samples and (b) microscopic images of typical process-induced defects (100x magnification), (b1) and (b2) fibre misalignment region, (b3) resin rich area, (c) microscopic image with pores highlighted in red (40x magnification), and (d) the whole cross-section with fibres in white and matrix in black (5x magnification). (For interpretation of the references to colour in this figure legend, the reader is referred to the web version of this article.)

ratio ν_{12} could be obtained as [39]:

$$\nu_{12} = -\varepsilon_2/\varepsilon_1 \qquad (1)$$

where the ε_2 was the strain transverse to the fibres, and the ε_1 denoted the strain along the fibres.

2.2.2. Three-point bending tests

Three-point bending tests were performed according to ASTM D790 [40]. The width of specimens was 12.7 mm, and the span to depth ratio was 16:1. Therefore, the spans for laminae with the thickness of 2 mm, 3 mm and 4 mm were 32 mm, 48 mm and 64 mm, respectively. The lengths were set to be 60 mm, 70 mm and 90 mm accordingly. The diameters of the indenter and support rollers in Fig. 7 (b) were all 10 mm. All specimens were tested at 0°. Isothermal bending tests were carried out at 1 mm/min until the strain reached 0.05 mm/mm or the samples broke before that.

2.2.3. Tension transverse to the fibres

When experiencing bending deformation, the specimens undergo a combination of geometrical and material nonlinearities, making the analysis difficult. In transverse tensions, all possible nonlinearities are from the material response. Specimens were cut according to ASTM D3039 [38] with a dimension of $175mm \times 25mm$. Isothermal tests were conducted at 2 mm/min until coupons broke.

2.3. Cyclic loading–unloading tests

There are few studies on mechanical properties and energy dissipation characteristics under cyclic loading–unloading conditions. Nevertheless, cyclic test data is essential to evaluate the reusable and damping performances of deployable structures based on SMPCs. It is the deformation, not the loading capacity that is the primary design parameter for deployable structures based on SMPCs. Therefore, cyclic straining with a constant and incremental strain amplitude was considered. In the constant loading–unloading tests (Fig. 8(a)), specimens were subjected to a constant strain amplitude of 0.025 mm/mm for fifteen loops. For incremental loading–unloading tests (Fig. 8(b)), specimens were subjected to three sets of five cycles, each set with increasing maximum strain: 0.01 mm/mm in solid lines, 0.03 mm/mm in dashed lines and 0.05 mm/mm in dotted lines. The SMPCs were deformed at or above the T_g, and the longitudinal tension was dominated by fibres with no hysteresis phenomenon. Therefore, the strain-controlled cyclic loading–unloading
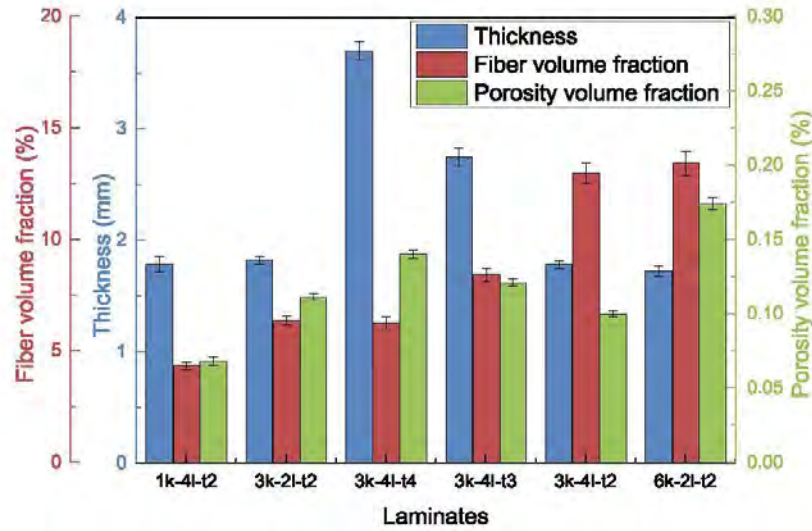
Fig. 6. Thickness, fibre volume fraction and porosity volume fraction of six kinds of laminae.
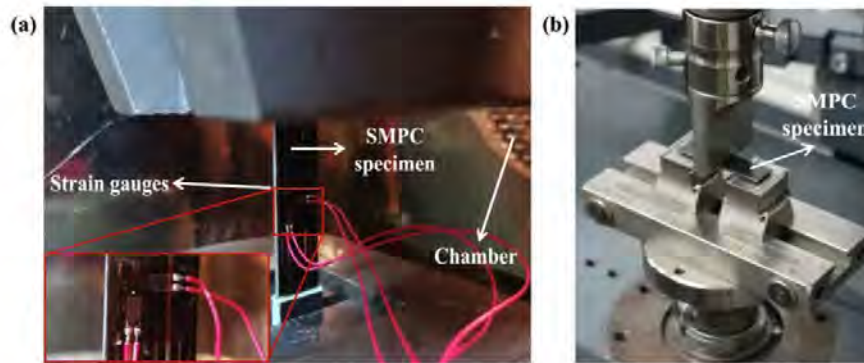

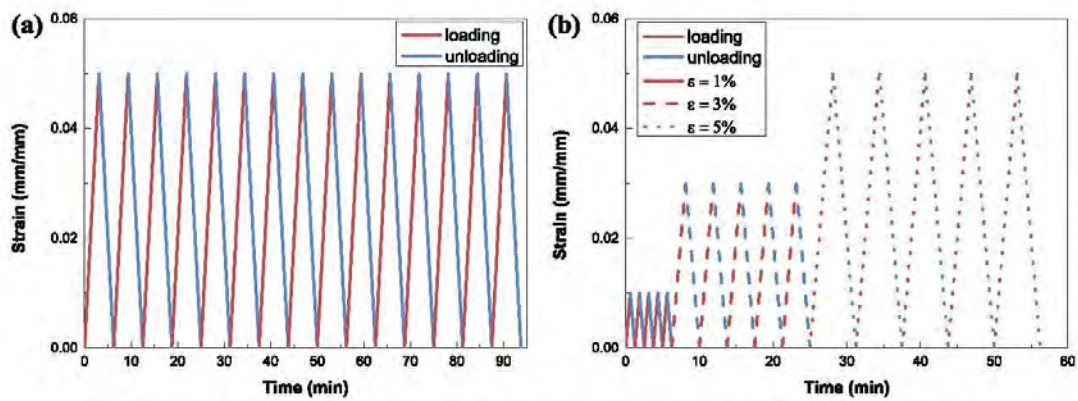**Fig. 7.** Experimental setup for (a) tensile tests and (b) three-point bending tests.

Fig. 8. The loading processes of cyclic tests for (a) constant loading–unloading and (b) incremental loading–unloading.

tests at 100 °C were carried out by three-point bending and transverse tension. The loading method was the same as that in monotonic tests. It should be noticed that sinusoidal loading is widely used in dynamic tests. Instead, the cyclic loading–unloading in this work is low-frequency and belongs to static tests. Therefore, the loading is applied in a triangular shape.

3. Results and discussion

3.1. Monotonic mechanical properties

3.1.1. Longitudinal tensile properties

Before analysing the tensile results of composites, we first detail the tensile properties of the polymer in Fig. 2 (b). The stress–strain curves show strong temperature dependence. At low temperatures (25 °C and 40 °C), the stresses increase rapidly with the strain, and the material shows brittle fracture. As the temperature rises, the material softens and the stresses drop by approximately two orders of magnitude. The elongation at break also presents obvious increases. However, when the temperature is higher than T_g, declines in elongation are observed. These drops can be illustrated by the rate-dependent properties of the viscoelastic characteristics. The fixed strain rate prevents the soft molecular chain segments from stretching sufficiently and thus the polymer breaks earlier [12].

Conversely, the longitudinal tensile stress–strain curves in Fig. 9 (a1–a6) demonstrate significant differences. The composites show brittle failure regardless of the temperature except for 3k-4l-t4 at 120 °C. It could be attributed to the pre-existing fibre misalignment (in Fig. 5), because the fibres in this thicker lamina are more vulnerable to moving during curing. Although according to the classical lamination theory (CLT), the matrix contributes little to the longitudinal tensile properties, the stress decreases with the temperature. The strength at temperatures around T_g is typically one-third to one-half of that at room temperature. This is because the bonding between fibres and matrix is perfect in CLT. However, the matrix becomes soft as the temperature rises, and the bonding between fibres and matrix is weakened, resulting in a declined fibre reinforcing effect [26]. At the same time, the elongation at break also presents a significant difference. When the temperature rises close to T_g, the elongation at the break of pure SMP increases by about 32 times. In contrast, the elongation at the break of these laminae shows a minor difference with the temperature. It is because, for UD lamina, the longitudinal tension is governed by fibres. Specifically, for laminae reinforced by 1k filament, the elongation at break is about 1.5 %, which is precisely the elongation of fibres. The elongation at break of laminae enhanced with 3k and 6k filaments is approximately 3.0 % and 3.5 %, respectively, which are approximately twice the elongation of the corresponding fibres. This inequality can be induced by the initial fibre waviness as shown in Fig. 4 (e1) – (e3). This waviness is prone to happen for thicker bundles because the width of grooves on the serrated edges in Fig. 4 (a) is 1 mm for a uniform distributed fibre assembly. This groove is as wide as the 1k bundle but narrower than the 3k and 6k bundles. Therefore, the fibres in laminae with 3k and 6k bundles are not perfectly tight and straight.

The longitudinal tensile modulus in Fig. 10 (a) also decreases by about 50 % with the increasing temperature. Besides, although technically, the modulus increases with the growth of fibre volume fraction, the rise in modulus is smaller than the growth in fibre content. This could be explained by the fibre–matrix interface, fibre distribution and misalignment. The imperfect bonding and random fibre waviness undermine the enhancing effect, and the degree of weakening is amplified in the thicker bundles and thicker laminae due to more potential misalignments. Additionally, Poisson's ratios in Fig. 10 (b) are all around 0.35, albeit some fluctuations exist, within the ranges of theoretical predictions in literature [31].

3.1.2. Three-point bending properties

The flexural stress σ_f, strain ε_f and secant modulus E_f can be calculated according to the ASTM D790 standard [40] as:

$$\sigma_f = \frac{3PL}{2bh^2} \tag{2}$$

$$\varepsilon_f = \frac{6\delta h}{L^2} \tag{3}$$

$$E_f = \frac{mL^3}{4bh^3} \tag{4}$$

In the above equations, P is the load; L is the support span; b represents the width; h denotes the thickness of the specimen; δ is the midspan deflection; m labels the slope of the secant of the force–deflection curves.

SMPC laminae exhibit stiffening responses at 25 °C and 40 °C in Fig. 9 (b1–b6). In these cases, cracks penetrate across the thickness under the indenter. As the temperature rises, the laminae yield at 60 °C and do not break before the maximum strain is attained except for thick coupons such as 3k-4l-t3 and 3k-4l-t4. The maximum stresses of the same laminae above 80 °C are about an order of magnitude lower than those at 25 °C. The flexural modulus and strength are depicted in Fig. 10 (c) and (d), respectively. Both first decrease sharply and then remain almost unchanged at above 80 °C, showing an order of magnitude reduction. The flexural modulus and strength present upward trends with fibre volume fraction at the same temperature. Nevertheless, the increasing proportion varies with the temperature, which is also caused by the weakened bonding at high temperatures. The augment of the flexural modulus compared with 1k-4l-t2 ($v_f = 4.32\%$) are 51.10 %, 28.95 %, 72.57 %, 108.13 %, 119.72 % at 25 °C, 40.91 %, 57.83 %, 51.90 %, 18.70 %, 83.98 % at 60 °C and 39.36 %, 45.76 %, 67.92 %, 64.72 %, 118.63 % at 100 °C for 3 k-2 l-t2 ($v_f = 6.36\%$), 3 k-4 l-t4 ($v_f = 6.24\%$), 3 k-4 l-t3 ($v_f = 8.42\%$), 3 k-4 l-t2 ($v_f = 12.97\%$) and 6 k-2 l-t2 ($v_f = 13.40\%$), respectively. Similarly, the growth of the flexural strength compared with 1 k-4 l-t2 ($v_f = 4.32\%$) are 47.40 %, 31.74 %, 69.9 %, 94.17 %, 136.89 % at 25 °C, 26.58 %, 17.71 %, 26.38 %, 17.72 %, 106.32 % at 60 °C and 53.82 %, 39.31 %, 53.82 %, 80.04 %, 95.43 % at 100 °C for 3 k-2 l-t2 ($v_f = 6.36\%$), 3 k-4 l-t4 ($v_f = 6.24\%$), 3 k-4 l-t3 ($v_f = 8.42\%$), 3 k-4 l-t2 ($v_f = 12.97\%$) and 6 k-2 l-t2 ($v_f = 13.40\%$), respectively. Besides, for laminae 3k-2l-t2 ($v_f = 6.36\%$) and 3k-4l-t4 ($v_f = 6.24\%$), their fibre volume fractions show a negligible difference. The latter presents a deteriorate enhancing effect due to the pre-existing waviness. Moreover, for 3k-4l-t2 ($v_f = 12.97\%$) and 6k-2l-t2 ($v_f = 13.40\%$), their fibre volume fractions and thicknesses are almost identical. Except for the fact that the modulus of 6k fibre bundles is 8.70 % higher than that of 3k fibre bundles, the effect of fibre microbuckling is also a significant factor. The 3k-4l-t2 lamina has four layers, which contribute to fibre microbuckling because the deflection depends on the position of fibres concerning the thickness direction [7], thus reducing flexural stiffness.

3.1.3. Transverse tensile properties

The transverse tensile stress–strain curves are shown in Fig. 9 (c1–c6). They are pretty similar to the tensile curves of the pure SMP in Fig. 2 (b). It has been reported that at low temperatures, molecular chains are "frozen" because the thermal motion energy of chain segments is not able to overcome the barrier of rotation in these chains. The interface between the fibres and matrix is sufficient to effectively transfer stress between matrix and reinforcement. Changes in bond lengths and angles caused by local vibrations of side groups, links and short chains, etc., will result in relatively high elastic moduli [41]. Therefore, when the experimental temperature is lower than T_g, the chain segment of the epoxy matrix can hardly move, and the brittle fracture occurs before yielding. As the temperature rises, the motion of chain segments is activated and the "frozen" molecular chains "thaw", resulting in a reduced load transfer efficiency of the fibre–matrix interface [41]. The ductile fracture similar to that of the matrix is observed at elevated temperatures. The mechanical properties decrease as the temperature rises. The elongation at break is also maximized when the temperature is close to the T_g. The transverse tensile modulus and strength in Fig. 10 (e) and (f) decrease by two and one order of magnitude, respectively. The
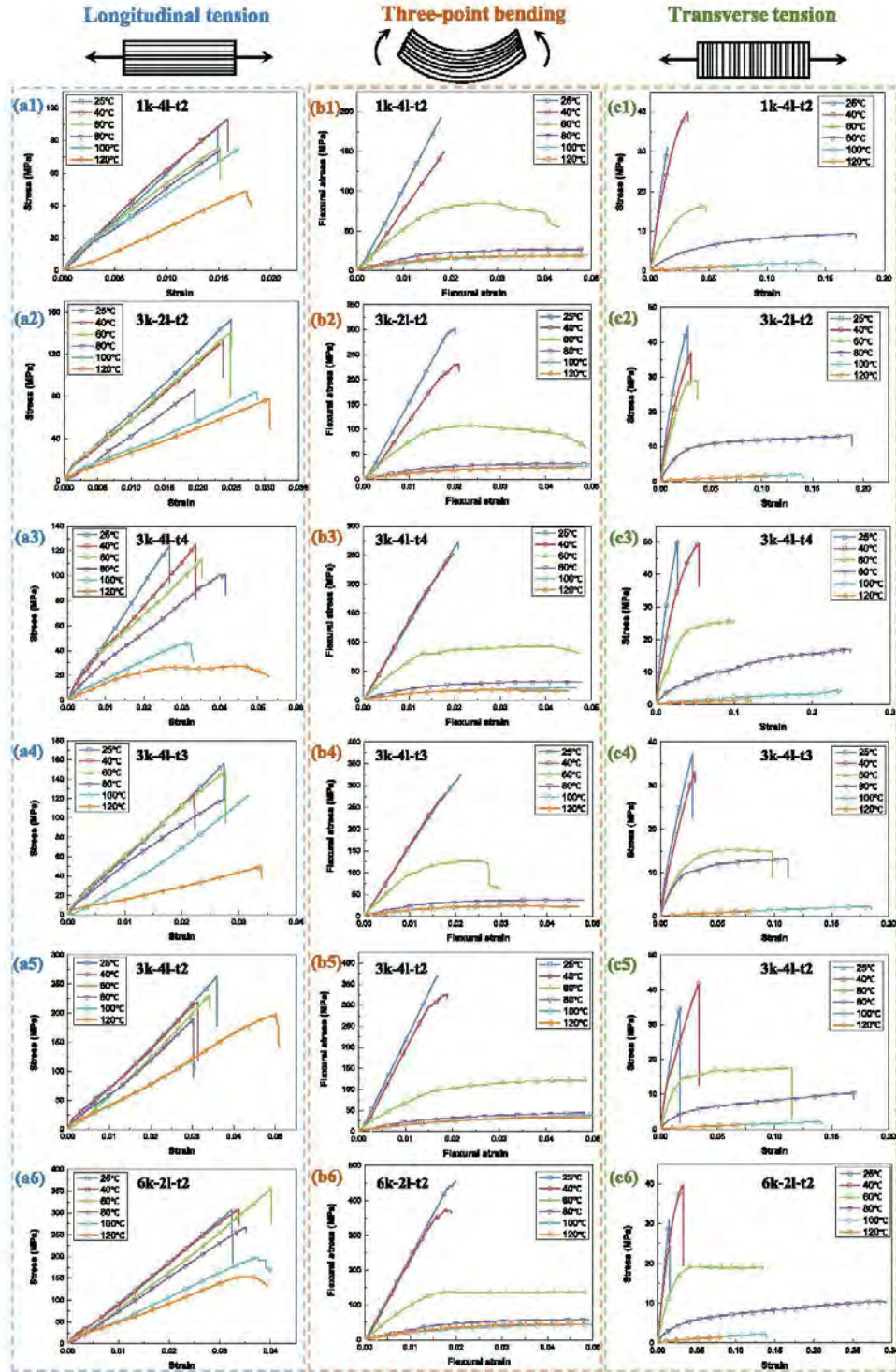
Fig. 9. Stress–strain curves from isothermal mechanical tests. (a) Longitudinal tension, (b) three-point bending and (c) transverse tension for (a1, b1, c1) 1k-4l-t2, (a2, b2, c2) 3k-2l-t2, (a3, b3, c3) 3k-4l-t4, (a4, b4, c4) 3k-4l-t3, (a5, b5, c5) 3k-4l-t2 and (a6, b6, c6) 6k-2l-t2.
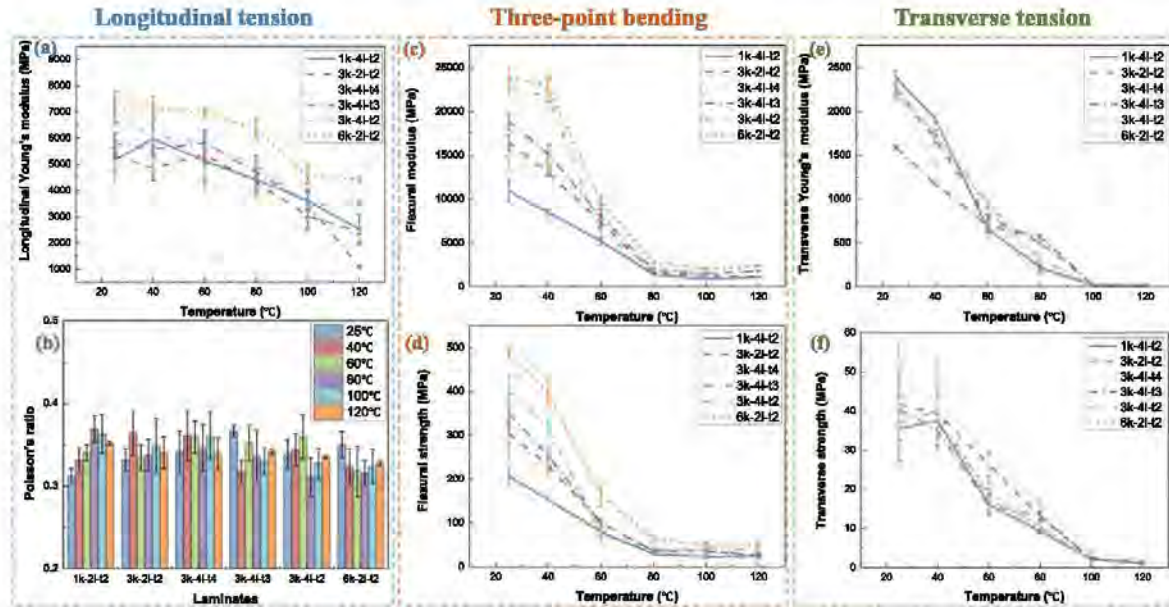
Fig. 10. Temperature-dependent mechanical properties. (a) Longitudinal tensile modulus, (b) Poisson's ratio, (c) flexural modulus, (d) flexural strength, (e) transverse tensile modulus and (f) transverse tensile strength.

transverse strength at low temperatures shows evident deviation among samples, which could be explained by fibre clustering. The fibre–matrix interface causes an increase in transverse tensile modulus but a decrease in strength compared with the matrix, as in the literature [42]. As the laminae studied in this work all possess relatively low fibre volume fractions, transverse tensile properties show limited differences among these samples.

3.2. Cyclic loading–unloading characteristics

The stress–strain curves under cyclic three-point bending and transverse tension tests are depicted in Fig. 11 (a-b) and (c-d), respectively. Different from composites with a standard epoxy matrix, the SMPCs at high temperatures are based on a rubber-like matrix. In the former case, failure is sudden. Instead, composites with super-elastic matrix are regarded to form stable microcracks that need additional load to propagate [43]. Therefore, they can retain much of their stiffness even after cracks have been formed. This can be illustrated by the misalignment of a few fibres in Fig. 5 (b) that can go across the path of the crack tears. These fibres can rotate and realign with the loading direction. Although these fibres are minority, they are able to sustain most of the load due to their high stiffness.

Some commonalities are found between the three-point bending and transverse tension conditions. Both loading and unloading branches are curvilinear with their curvatures in opposite directions, forming significant hysteresis. The hysteresis can be attributed to two factors: the viscoelastic relaxation effect [44] and the Mullins effect [45]. The stress in the reloading process is smaller than the response of the initial loading until surpassing the applied strain amplitude as in literature [46]. The Mullins effect is caused by the debonding between the matrix and enhancement, and this detachment mainly occurs in the virgin samples, i.e. the first cycles [47]. The hysteresis is more pronounced with high strain amplitudes, showing a strain amplitude-dependent characteristic. Besides, the mean stress decreases and approaches an asymptotic value as the cycle continues. For constant loading–unloading tests in Fig. 11 (a) and (c), the reduction of stress is largest between the first and second cycle and remains almost unchanged after three cycles, this is the so-

called preconditioning [48–50]. A similar pattern is observed in incremental loading–unloading tests in Fig. 11 (b) and (d), while a corresponding increase in stress reduction at each increase in strain amplitude is detected. Additionally, as the cycles proceed, the loading start points and unloading endpoints show downward shifts. Specifically, the endpoints become negative because the tests are strain-controlled and no residual stretch is seen in Fig. 8. This can be attributed to the lagging movement of the chain segment due to the viscoelasticity, and the induced plastic deformation [51,52]. However, the shift rate decreases with the increasing number of cycles and tends to zero after about four and two cycles for three-point bending and transverse tension, respectively.

On the other hand, there are some discrepancies in stress–strain curves between the three-point bending and transverse tension loadings. It is noticed that during the entire cyclic process in transverse loading conditions, the slopes of the loading and unloading curves remain almost constant, indicating an insignificant stiffness reduction. The hysteresis loops of transverse tensions are slimmer and more stable, showing less nonlinearity. These differences are because the possible source of nonlinearity in transverse tension is simply the material response. However, the bending experiments combine both the geometrical (fibre microbuckling) and material (viscoelasticity) nonlinearities. In addition, the stress–strain response tends to stabilise as the cycle progresses, while the degree and rate of stabilisation vary. For three-point bending tests, the offset between adjacent loops decreases, especially from the second loop. However, a clear non-overlap can be seen even if it reaches the fifteenth cycle. Conversely, the curves in the second loop in transverse tension show a saturated stress–strain response.

Macroscopic images of samples after constant cyclic three-point bending tests in Fig. 12 show that the specimen almost completely recovered. There are non-visible cracks on lateral and stretched surfaces, while crushed epoxy matrix is observed on the compressed surface. The fibre microbuckling, delamination and damage of matrix caused by repeated usages have been reported by Zhang et.al [53]. Therefore, in order to investigate the possible fibre failure, matrix cracking, or the debonding of fibre–matrix interface caused by repeated bending and
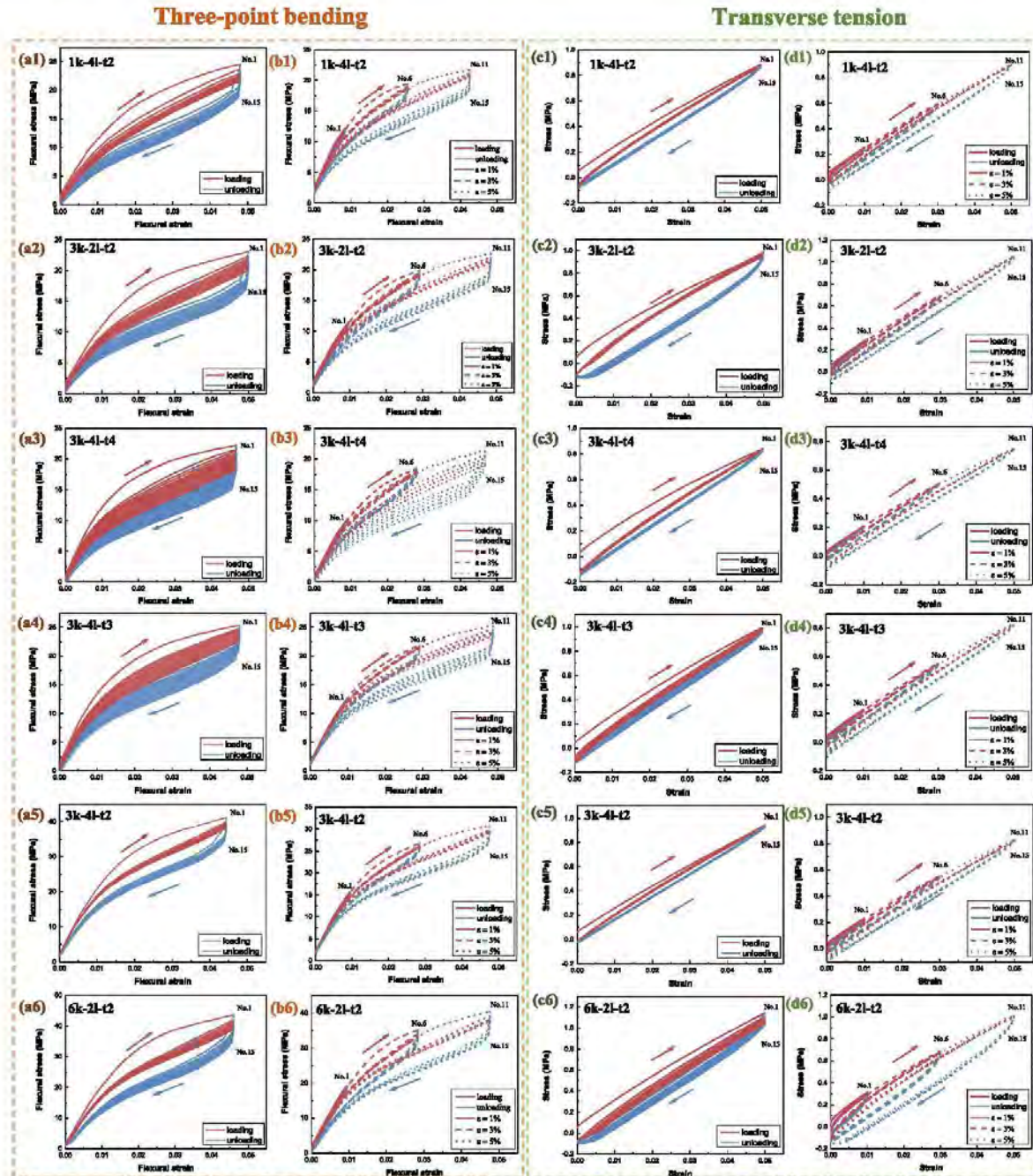
Three-point bending   **Transverse tension**

Fig. 11. Cyclic loading–unloading curves at 100 °C. (a) Three-point bending of fifteen cycles with the maximum flexural strain of 0.05 mm/mm, (b) three-point bending of five cycles with the flexural strain ranges of 0.01 mm/mm, 0.03 mm/mm and 0.05 mm/mm, respectively, (c) transverse tension of fifteen cycles with the strain of 0.05 mm/mm and (d) transverse tension of five cycles with the strain ranges of 0.01 mm/mm, 0.03 mm/mm and 0.05 mm/mm, respectively, for (a1, b1, c1 and d1) 1k-4l-t2, (a2, b2, c2 and d2) 3k-2l-t2, (a3, b3, c3 and d3) 3k-4l-t4, (a4, b4, c4, and d4) 3k-4l-t3, (a5, b5, c5, and d5) 3k-4l-t2 and (a6, b6, c6, and d6) 6k-2l-t2 (the red arrow represents the loading direction and the blue one embodies the unloading direction). (For interpretation of the references to colour in this figure legend, the reader is referred to the web version of this article.)
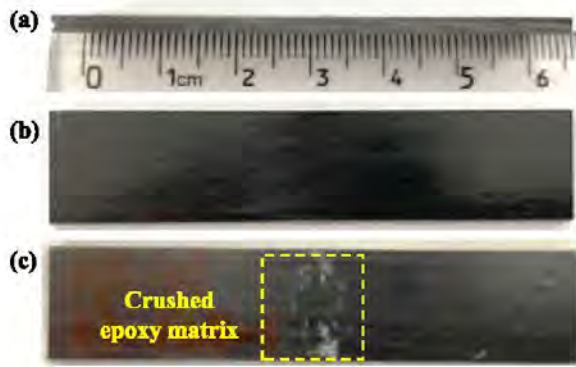
(a)

(b)

(c) Crushed epoxy matrix

Fig. 12. Macroscopic images of samples after constant cyclic three-point bending tests, (a) lateral surface, (b) stretched surface and (c) compressed surface.

recovery, morphologies of lateral and compressed surfaces of samples that have undergone constant cyclic three-point bending tests were characterised by a scanning electron microscope (SEM) (ZIESS Ultra-55) at 10 kV.

The lateral surfaces of six sets of samples are shown in Fig. 13, with their cross-sections magnified 30 × and highly-compressed region magnified 500 × . The lateral surfaces of 1k-4l-t2 in Fig. 13 (a), and 3k-2l-t2 in Fig. 13 (b) are almost intact, while microcracks are observed in

laminae with larger thicknesses and higher fibre volume fractions. The typical widths of microcracks are 5.03 μm, 4.26 μm, 2.71 μm and 5.63 μm for 3k-4l-t2, 3k-4l-t3, 3k-4l-t2 and 6k-4l-t2 laminae, respectively. It is concluded that the width increases with the laminae thickness and fibre volume fraction. For 3k-4l-t2 and 6k-4l-t2 with almost the same thickness and fibre volume fraction, the cracks width of 3k-4l-t2 is only half of that of 6k-4l-t2. This result is consistent with the finite element analysis [28], where the matrix strain is greater in models with high fibre aggregation.

The compressed surfaces are shown in Fig. 14, with fibre failure and fibre–matrix interface differentiated at high magnifications 500 × . The cracks of 1k-4l-t2 and 3k-2l-t2 in Fig. 14 (a) and (b), respectively, are insignificant, of which the widths are less than 30 μm. Significant cracks and crushed matrix are detected on 3k-4l-t4 in Fig. 14 (c). The fibre failure observed in Fig. 14 (c5) and (c6) inclines with an angle (β) to the fibre direction, which was also found in other laminates [54]. Exposed fibres associated with matrix ridges and valleys implies the occurrences of fibre–matrix debonding [55]. The shear cusps characterise the matrix cracking due to the highly-microbuckled fibres. The crushed epoxy matrix is observed in Fig. 14 (d-f), of which the typical crack widths are 94.38 μm for 3k-4l-t3, 22.23 μm for 3k-4l-t2 and 204.38 μm for 6k-2l-t2.

The area under the loading curve is the total work that the cyclic load has done and represents the total strain energy W_t. Whereas the area under the unloading curve represents the elastic strain energy W_e which is reversible, indicating the work transformed into the energy stored in samples. The dissipated energy W_d is evaluated by the area between the loading and unloading curves [56]. This dissipative phenomenon can be explained by several factors such as (i) damping of the viscoelastic
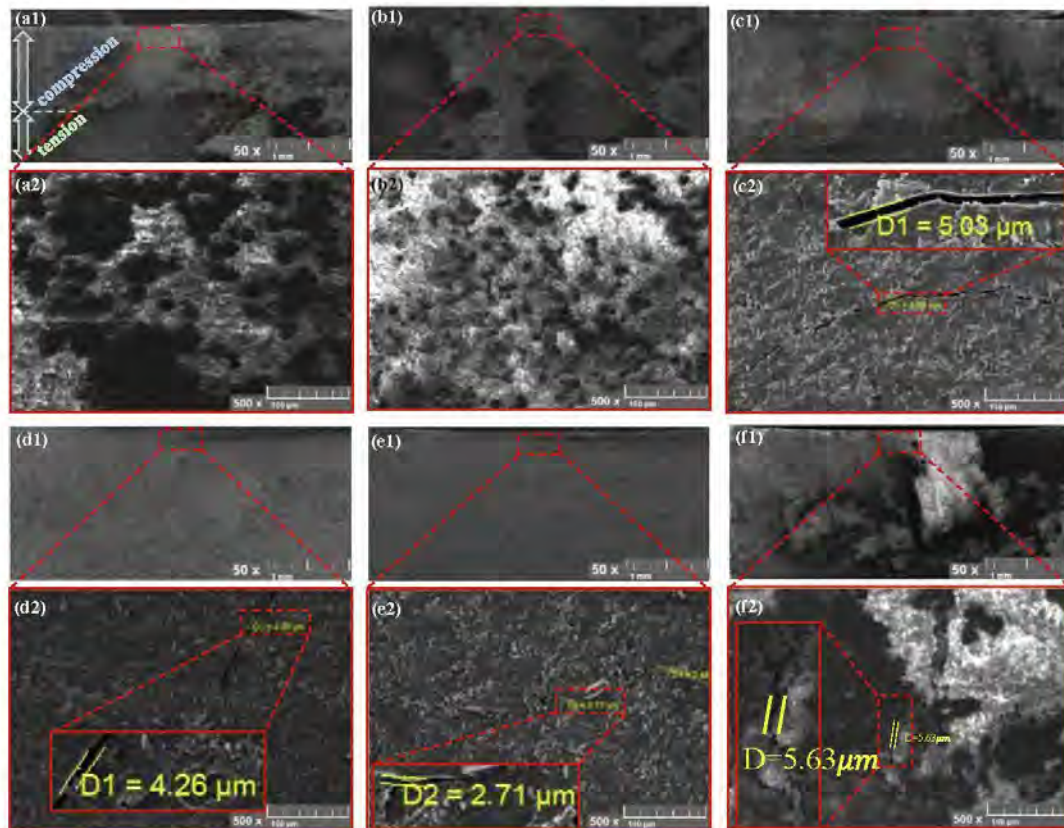

Fig. 13. SEM images of lateral surfaces after constant cyclic three-point bending tests, (a) 1k-4l-t2, (b) 3k-2l-t2, (c) 3k-4l-t4, (d) 3k-4l-t3, (e) 3k-4l-t2 and (f) 6k-2l-t2, for (a1, b1, c1, d1, e1, f1) at 50 × magnification, (a2, b2, c2, d2, e2, f2) at 500 × magnification.
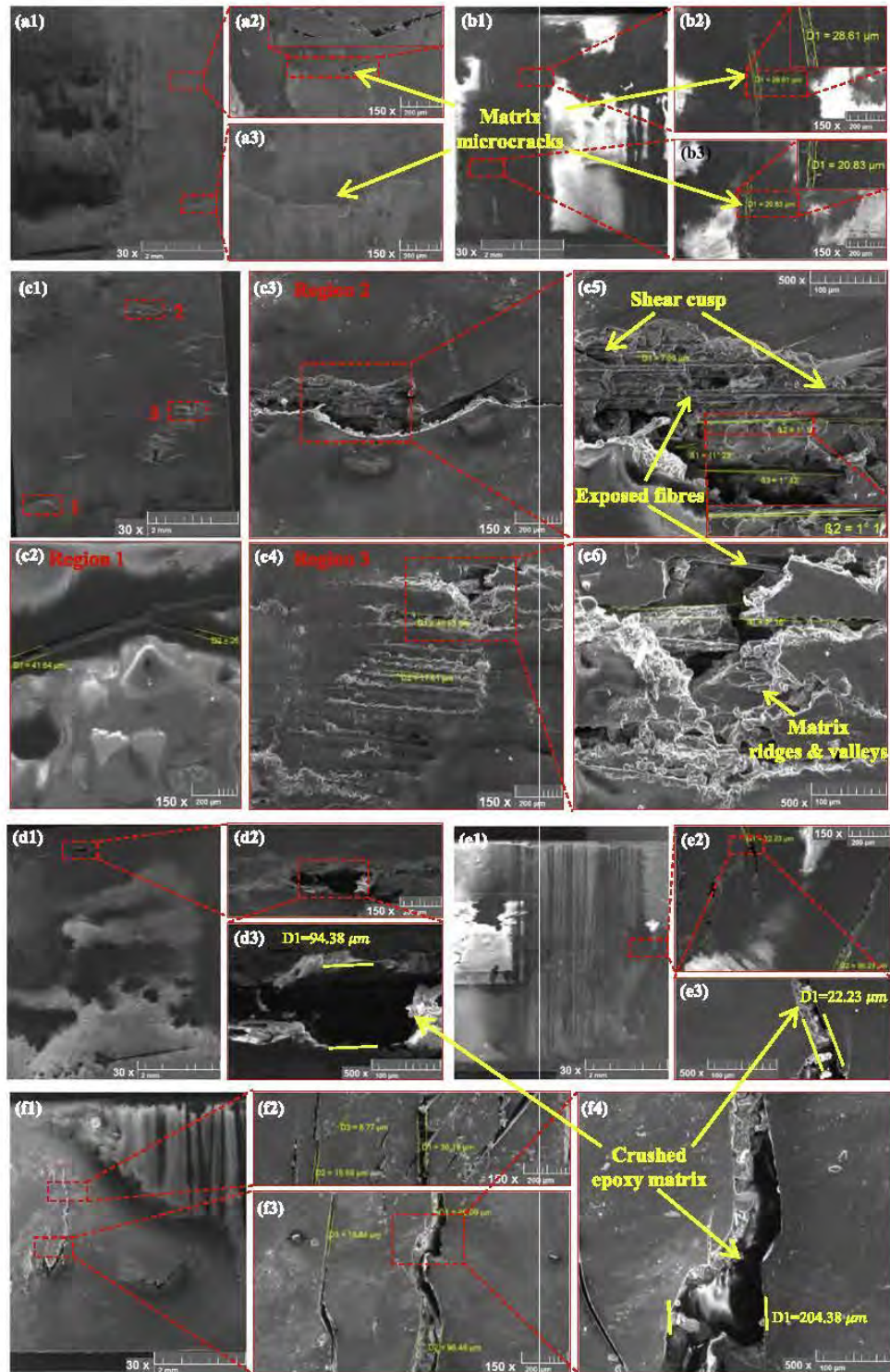
Fig. 14. SEM images of compressed surfaces after constant cyclic three-point bending tests, (a) 1k-4l-t2, (b) 3k-2l-t2, (c) 3k-4l-t4, (d) 3k-4l-t3, (e) 3k-4l-t2 and (f) 6k-2l-t2, for (a1, b1, c1, d1, e1, f1) at 30 × magnification, (a2, a3, b2, b3, c2, c3, c4, d2, e2, f2, f3) at 150 × magnification and (c5, c6, d3, e3, f4) at 500 × magnification.

matrix, (ii) the fibre–fibre friction, (iii) the debonding between fibres and matrix and (iv) deformation or reorientation of fibres [48]. The final one is strongly affected by the initial fibre misalignment or waviness, and microbuckling when samples undergo bending deformation. Exposed fibres in Fig. 14 (c5) and (c6) indicates the fibre deformation due to the microbuckling behaviour of typical flexible composites. This phenomenon is believed to favour the wrinkling which will further affect the fibre–matrix debonding and enhance the nonlinearity [57,58]. In addition, the loss factor η is defined as the ratio of the dissipated energy W_d to total strain energy W_t, representing energy dissipation characteristics of the specimen during each cycle:

$$\eta = W_d / W_t \tag{4}$$

The stiffness loss k can be calculated as:

$$k = \sigma / \sigma_0 \tag{5}$$

where σ is the maximum stress of every cycle and σ_0 denotes the maximum stress in the first cycle.

The total strain energy in Fig. 15 (a1), (b1), (c1) and (d1) shows an about 15 % drop in the second cycle and continues to decrease as the cycle proceeds. The elastic strain energy in Fig. 15 (a2), (b2), (c2) and (d2) presents a similar pattern, but without the apparent drop at the beginning. However, the dissipated energy in Fig. 15 (a3), (b3), (c3) and (d3) is a little different. This energy exhibits a minimum value in the second cycle and then stabilises. These three energies corresponding to the first cycle are significantly higher due to initial defects and structural instability. From the second cycle, the shape of the hysteresis loops in Fig. 11 becomes regular, and these three strain energies stabilise. These energies are strongly correlated with the strain amplitude and fibre volume fraction. Nevertheless, for dissipated energy, some exceptions are found in transverse tension. The energies dissipated in 3k-2l-t2 and 3k-4l-t2 are significantly higher and lower than expected, respectively.
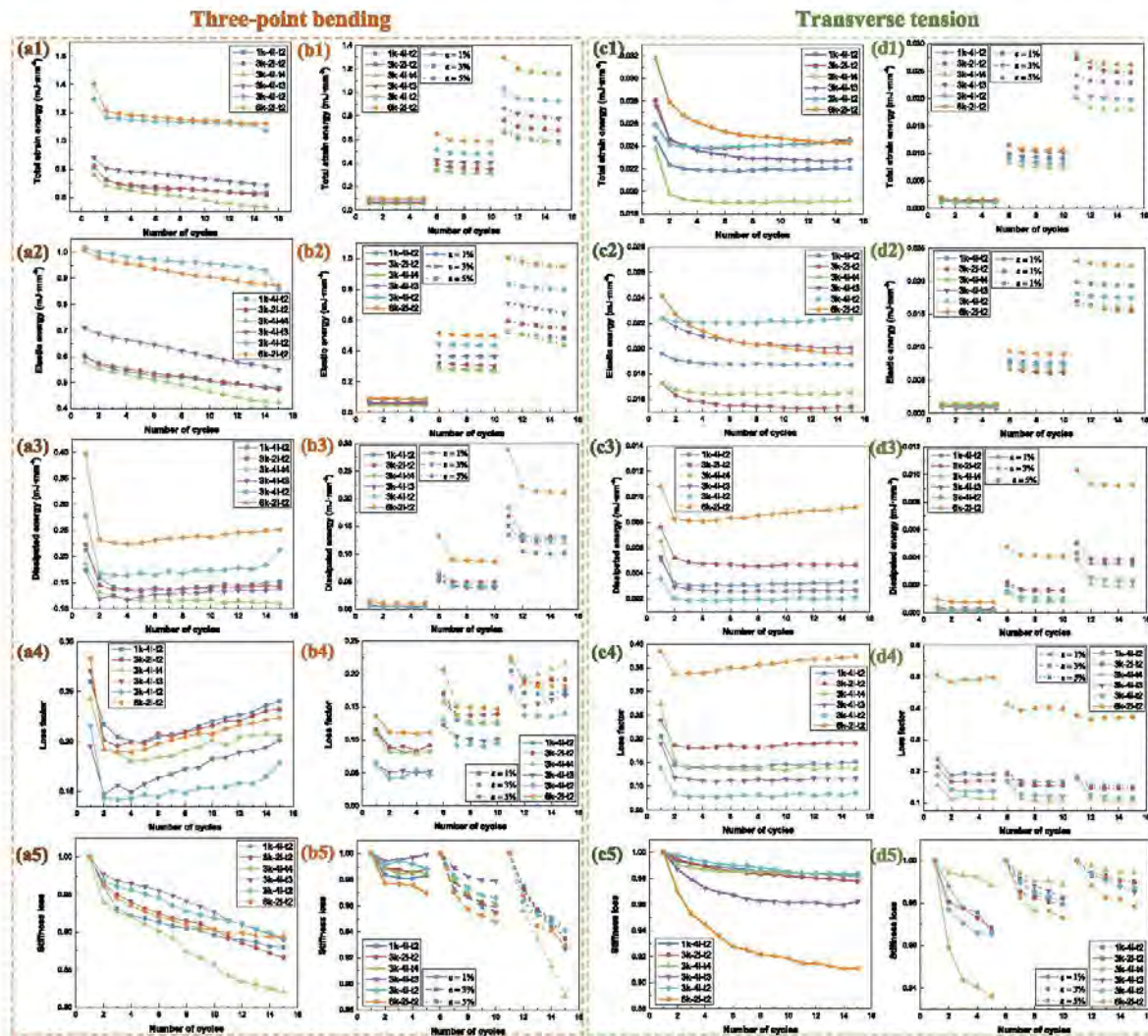

Fig. 15. Cyclic loading–unloading properties vary with the number of cycles. (a) Three-point bending of constant cycles with the flexural strain of 0.05 mm/mm, (b) three-point bending of incremental cycles with the flexural strains of 0.01 mm/mm, 0.03 mm/mm and 0.05 mm/mm, (c) transverse tension of constant cycles with the strain of 0.05 mm/mm and (d) transverse tension of incremental cycles with the strains of 0.01 mm/mm, 0.03 mm/mm and 0.05 mm/mm. For total strain energy in (a1), (b1), (c1) and (d1); elastic energy in (a2), (b2), (c2) and (d2); dissipated energy in (a3), (b3), (c3) and (d3); loss factor in (a4), (b4), (c4), and (d4); and stiffness loss in (a5), (b5), (c)5 and (d5).

These anomalies are caused by fibre distribution. Fibre clustering is more pronounced in 3k-2l-t2, resulting in more intense fibre–fibre friction and a less robust fibre–matrix interface. Therefore, more energy is consumed. Contrariwise, compared with 6k-2l-t2, the fibres are more dispersed in 3k-4l-t2. Therefore, although they have almost the same fibre volume fraction, the energy expended by the friction and debonding in 3k-4l-t2 is conserved.

The loss factor maximizes in the first cycle and minimizes in the second or third cycle, followed by a slight increase. The reason for this first decline is the initiation of microcracks. Besides, there is no monotonic relationship between the loss factor and fibre volume fraction. We take the 1k-4l-t2, 3k-4l-t2 and 6k-2l-t2 for illustration. The 1k-4l-t2 lamina possesses the lowest fibre volume fraction but presents a leading loss factor, even the highest one in the constant three-point bending (Fig. 15 (a4)). It should be noticed that the matrix at the rubbery state has a high damping ratio and such lamina with the highest matrix volume fraction dissipates more energy, which results in higher loss factors. As the fibre volume fraction increases, the effect of microcracks overtakes the viscoelasticity [26]. However, the 3k-4l-t2 and 6k-2l-t2 have almost the same fibre volume fraction, but almost the lowest and highest loss factor, respectively. This can be illustrated by the different degrees of fibre clustering. The 6k reinforcement is stouter than the 3k one, and therefore, the fibres in 6k-2l-t2 are more unevenly distributed. In three-point bending, the fibre microbuckling tends to occur in laminae with uniform fibre distribution, and thus reduces the damping ratio. This can be seen in Fig. 14 (e) and (f), where cracks on 3k-4l-t2 compressed surface are less significant and less widely distributed than those on 6k-2l-t2. In transverse tension, the homogeneous distribution of fibres mitigates the initiation of microcracks.

Some differences are observed between the three-point bending and transverse tension. Firstly, the convergence speed is different. In three-point bending tests, the loss factor stabilises after the fourth cycle in constant loading (Fig. 15 (a4)) and steadies after the second cycle in incremental cycles (Fig. 15 (b4)). However, it soothes faster under the transverse tensions, after the second cycle in both constant and incremental loadings (Fig. 15 (c4) and (d4)). Then, a more obvious increase caused by the internal friction [59] is observed in three-point-bending, because the internal stress is more complex. Besides, the loss factor for incremental cyclic tests in three-point bending in Fig. 15 (b4) and transverse tension in Fig. 15 (d4) show opposite trends with the strain amplitude. In three-point bending, the loss factor climbs with the strain amplitude, because the microbuckling behaviour of carbon fibres magnifies when the strain amplitude enlarges. The more intense waviness induces greater deformation in the matrix and thus weakens the fibre–matrix bonding in laminae. Conversely, in the transverse tension, it shrinks due to the attenuation of the microcrack growth because of the former training experiences [26].

A significant loss in stiffness in Fig. 15 (a5), (b5), (c5) and (d5) is detected after the first loop to a given strain amplitude, followed by a slight drop in the rest of the cycle. Some differences appear between the three-point bending and transverse tension. First, the degree of stiffness loss varies, and the material corresponding to the maximum stiffness loss is also different. For instance, in constant cyclic tests, the stiffness loss maximizes in 3k-4l-t4 at about 82 % in three-point bending (Fig. 15 (a5)). Fibre microbuckling is the mechanism to achieve large bending deformations at the expense of stiffness and is highly sensitive to lamina thickness. Therefore, the fibre waviness is more violent in these thicker samples at the same flexural strain, which is verified by SEM observations in Fig. 14, where fibre fracture is only detected on the compressed surface of 3k-4l-t4 lamina. However, the maximal stiffness loss reaches about 91 % in 6k-2l-t2 when subjected to transverse tension (Fig. 15 (c5)). This stouter bundle with six thousand fibre monofilaments causes higher porosity volume fraction in Fig. 6 and initiates more microcracks. Then, the stiffness loss for incremental cyclic tests in three-point bending and transverse tension shows opposite trends with the strain amplitude. In the three point bending in Fig. 15 (b5), the stiffness loss grows with

the strain amplitude. Conversely, in the transverse tension in Fig. 15 (d5), it diminishes with the strain amplitude. The reason is the same as that for the loss factor. Additionally, the determinant of stiffness loss varies as the strain amplitude increases. For three-point bending results, the stiffness loss is dominated by viscoelastic properties of the matrix in laminae with low fibre volume fraction (1k-4l-t2) and microcracks with high fibre volume fraction (3k-4l-t3 & 6k-2l-t2) when the flexural strain is 1 % and 3 % in Fig. 15 (b5). However, the effect of the lamina thickness (3k-4l-t4) becomes significant when the flexural strain grows to 5 %. This is because the thickness has a greater effect on fibre microbuckling than fibre volume fraction [7]. The fibre microbuckling occurs after a critical bending curvature, and after that, the nonlinearity originating from this instability exceeds that from viscoelasticity and microcracks. For transverse tension, the stiffness losses for 3k-4l-t4 and 6k-2l-t2 are the smallest and biggest, respectively, in both constant and incremental cycles. The corresponding reasons are the matrix's large strain capacity and microcracks caused by the fibre clustering.

4. Conclusions

The effect of the reinforcement, lamina thickness, fibre volume fraction and distribution on mechanical properties, especially nonlinear and reusable responses of SMPCs have been investigated by both the monotonic and fifteen cyclic loading–unloading tests, in forms of the longitudinal tension, three-point bending and transverse tension. Samples fabricated by the modified manual winding method are characterised by an optical microscope with negligible porosity volume fraction. Conclusions can be drawn in two aspects.

- The monotonic tests show temperature-dependent results. The moduli and strengths decrease with temperature and increase with fibre volume fraction. The reinforcing effect is also undermined as the temperature rises because the bonding between fibres and matrix weakens when SMPs are in a rubbery state.
- The cyclic loading–unloading tests demonstrate softening and hysteresis characteristics. This nonlinear response is strain amplitude-dependent but does not always increase with the growth of fibre volume fraction. For composites with low fibre volume fractions, the loss factor and stiffness loss are dominated by the matrix's damping properties and decrease with the fibre volume fraction. As the fibre volume fraction increases, the effect of microcracks becomes more significant. Besides, differences are observed between the bending and transverse tension. For three-point bending, the nonlinearity is dominated by the matrix and fibre volume fraction at small flexural strains but determined by the fibre microbuckling behaviour at higher strains. For transverse tension, the degree of fibre clustering has a greater influence because it affects the bonding between the matrix and fibres. The higher the degree of concentration, the more pronounced the loss factor and stiffness loss.

The contribution of this work is not only to offer experimental data of the fabricated UD carbon fibre-reinforced SMPCs but to disseminate valuable findings for material design in engineering applications. The reusability of SMPCs based deployable structures is a feature that makes them superior to explosive mechanisms. Therefore, apart from the lamina thickness and fibre volume fraction, which are two traditional design parameters, more attention should be paid to the degree of fibre clustering. Samples with evenly distributed fibres show reduced loss factor and stiffness loss, and present more stable mechanical performance, although their preparation is more labour-intensive. Besides, the cyclic loading-unloading results can also promote research in fibre–matrix interface modelling and progressive damage analysis.

CRediT authorship contribution statement

Dou Zhang: Methodology, Validation, Investigation, Data curation,

Visualization, Writing – original draft, Writing – review & editing. **Liwu Liu:** Project administration, Writing – review & editing. **Xin Lan:** Investigation, Conceptualization, Funding acquisition. **Fengfeng Li:** Writing – review & editing, Funding acquisition. **Yanju Liu:** Resources, Writing – review & editing, Supervision. **Jinsong Leng:** Resources, Funding acquisition, Supervision.

Declaration of Competing Interest

The authors declare that they have no known competing financial interests or personal relationships that could have appeared to influence the work reported in this paper.

Data availability

Data will be made available on request.

Acknowledgements

References

[1] Liu T, Zhou T, Yao Y, Zhang F, Liu L, Liu Y, et al. Stimulus methods of multi-functional shape memory polymer nanocomposites: A review. Compos Part A Appl Sci Manuf 2017;100:20–30. https://doi.org/10.1016/j.compositesa.2017.04.022.

[2] Gu J, Zhang X, Duan H, Wan M, Sun H. A hygro-thermo-mechanical constitutive model for shape memory polymers filled with nano-carbon powder. Int J Smart Nano Mater 2021;12:286–306.

[3] Zhang F, Wen N, Wang L, Bai Y, Leng J. Design of 4D printed shape changing tracheal stent and remote controlling actuation. Int J Smart Nano Mater 2021;12: 375–89.

[4] Che D, Saxena I, Han P, Guo P, Ehmann KF. Machining of carbon fiber reinforced plastics/polymers: a literature review. J Manuf Sci Eng 2014;136. https://doi.org/10.1115/1.4026526.

[5] Leng J, Lan X, Liu Y, Du S. Shape-memory polymers and their composites: Stimulus methods and applications. Prog Mater Sci 2011;56:1077–135. https://doi.org/10.1016/j.pmatsci.2011.03.001.

[6] Liu T, Liu L, Yu M, Li Q, Zeng C, Lan X, et al. Integrative hinge based on shape memory polymer composites: Material, design, properties and application. Compos Struct 2018;206:164–76. https://doi.org/10.1016/j.compstruct.2018.08.041.

[7] Lan X, Liu L, Liu Y, Leng J, Du S. Post microbuckling mechanics of fibre-reinforced shape-memory polymers undergoing flexure deformation. Mech Mater 2014;72: 46–60. https://doi.org/10.1016/j.mechmat.2013.05.012.

[8] Liu Y, Du H, Liu L, Leng J. Shape memory polymers and their composites in aerospace applications: A review. Smart Mater Struct 2014. https://doi.org/10.1088/0964-1726/23/2/023001.

[9] Li F, Liu L, Lan X, Pan C, Liu Y, Leng J, et al. Ground and geostationary orbital qualification of a sunlight-stimulated substrate based on shape memory polymer composite. Smart Mater Struct 2019;28:075023. https://doi.org/10.1088/1361-665X/ab18b7.

[10] Lan X, Liu LW, Zhang FH, Liu ZX, Wang LL, Li QF, et al. World's first spaceflight on-orbit demonstration of a flexible solar array system based on shape memory polymer composites. Sci China Technol Sci 2020;63:1436–51. https://doi.org/10.1007/s11431-020-1681-0.

[11] Yarali E, Taheri A, Baghani M. A comprehensive review on thermomechanical constitutive models for shape memory polymers. J Intell Mater Syst Struct 2020;31: 1243–83. https://doi.org/10.1177/1045389X20916795.

[12] Chen J, Liu L, Liu Y, Leng J. Thermoviscoelastic shape memory behavior for epoxy shape memory polymer. Smart Mater Struct 2014;23:055025. https://doi.org/10.1088/0964-1726/23/5/055025.

[13] Liu Y, Gall K, Dunn ML, Greenberg AR, Diani J. Thermomechanics of shape memory polymers: Uniaxial experiments and constitutive modeling. Int J Plast 2006;22:279–313. https://doi.org/10.1016/j.ijplas.2005.03.004.

[14] Pan Z, Zhou Y, Zhang N, Liu Z. A modified phase based constitutive model for shape memory polymers. Polym Int 2018;67:1677–83.

[15] Qi HJ, Nguyen TD, Castro F, Yakacki CM, Shandas R. Finite deformation thermo-mechanical behavior of thermally induced shape memory polymers. J Mech Phys Solids 2008;56:1730–51.

[16] Kim JH, Kang TJ, Yu W-R. Thermo-mechanical constitutive modeling of shape memory polyurethanes using a phenomenological approach. Int J Plast 2010;26: 204–18.

[17] Guo X, Liu L, Zhou B, Liu Y, Leng J. Constitutive model for shape memory polymer based on the viscoelasticity and phase transition theories. J Intell Mater Syst Struct 2016;27:314–23.

[18] Zhao F, Zheng X, Zhou S, Zhou B, Xue S, Zhang Y. Constitutive model for epoxy shape memory polymer with regulable phase transition temperature. Int J Smart Nano Mater 2021;12:72–87.

[19] Heinrich C, Aldridge M, Wineman AS, Kieffer J, Waas AM, Shahwan K. The influence of the representative volume element (RVE) size on the homogenized response of cured fiber composites. Model Simul Mater Sci Eng 2012;20:075007. https://doi.org/10.1088/0965-0393/20/7/075007.

[20] López JF. On the isotropy of randomly generated representative volume elements for fiber-reinforced elastomers. Compos Part B Eng 2016;87:33–9. https://doi.org/10.1016/j.compositesb.2015.10.014.

[21] Zhang J, Dui G, Wang X. Post-micro-buckling of carbon fibers in functionally graded plates under pure bending. Eur J Mech A/Solids 2019;75:419–25. https://doi.org/10.1016/j.euromechsol.2019.02.007.

[22] Diani J, Gilormini P, Frédy C, Rousseau I. Predicting thermal shape memory of crosslinked polymer networks from linear viscoelasticity. Int J Solids Struct 2012; 49:793–9. https://doi.org/10.1016/j.ijsolstr.2011.11.019.

[23] Sujithra R, Srinivasan SM, Arockiarajan A. Shape recovery studies for coupled deformations in an epoxy based amorphous shape memory polymers. Polym Test 2015;48:1–6. https://doi.org/10.1016/j.polymertesting.2015.09.005.

[24] Du H, Liu L, Zhang F, Zhao W, Leng J, Liu Y. Thermal-mechanical behavior of styrene-based shape memory polymer tubes. Polym Test 2017;57:119–25. https://doi.org/10.1016/j.polymertesting.2016.11.011.

[25] Francis WH, Lake MS, Schultz MR, Campbell D, Dunn M, Jerry QH. Elastic memory composite microbuckling mechanics: Closed-form model with empirical correlation. Collect Tech Pap - AIAA/ASME/ASCE/AHS/ASC Struct Struct Dyn Mater Conf 2007;6:5531–46. https://doi.org/10.2514/6.2007-2164.

[26] Li F, Scarpa F, Lan X, Liu L, Liu Y, Leng J. Bending shape recovery of unidirectional carbon fiber reinforced epoxy-based shape memory polymer composites. Compos Part A Appl Sci Manuf 2019;116:169–79. https://doi.org/10.1016/j.compositesa.2018.10.037.

[27] Diani J, Fayolle B, Gilormini P. A review on the Mullins effect. Eur Polym J 2009; 45:601–12. https://doi.org/10.1016/j.eurpolymj.2008.11.017.

[28] López Jiménez F, Pellegrino S. Folding of fiber composites with a hyperelastic matrix. Int J Solids Struct 2012;49:395–407. https://doi.org/10.1016/j.ijsolstr.2011.09.010.

[29] Qi Y, Caillard J, Long R. Fracture toughness of soft materials with rate-independent hysteresis. J Mech Phys Solids 2018;118:341–64. https://doi.org/10.1016/j.jmps.2018.05.020.

[30] Long R, Hui C-Y. Fracture toughness of hydrogels: measurement and interpretation. Soft Matter 2016;12:8069–86.

[31] Li F, Leng J, Liu Y, Remillat C, Scarpa F. Temperature dependence of elastic constants in unidirectional carbon fiber reinforced shape memory polymer composites. Mech Mater 2020;148:103518. https://doi.org/10.1016/j.mechmat.2020.103518.

[32] Leng J, Wu X, Liu Y. Effect of a linear monomer on the thermomechanical properties of epoxy shape-memory polymer. Smart Mater Struct 2009;18:095031. https://doi.org/10.1088/0964-1726/18/9/095031.

[33] Sheng SZ, Van Hoa S. Three dimensional micro-mechanical modeling of woven fabric composites. J Compos Mater 2001;35:1701–29. https://doi.org/10.1106/PYIX-4V9P-RE9L-LDNE.

[34] Zhang D, Liu L, Lan X, Leng J, Liu Y. Synchronous deployed design concept triggered by carbon fibre reinforced shape memory polymer composites. Compos Struct 2022;290:115513. https://doi.org/10.1016/j.compstruct.2022.115513.

[35] Minjie Z, Shuhong X. Review of recent advances in pyroshock for space system. Vibroengineering Procedia 2014;4:86–90.

[36] Joyce PJ, Moon TJ. Compression strength reduction in composites with in-plane fiber waviness. ASTM Spec Tech Publ 1998;1330:76–96.

[37] Francis WH. Mechanics of post-microbuckled compliant-matrix composites; 2008.

[38] INTERNATIONAL A. Standard test method for tensile properties of polymer matrix composite materials. Annu B ASTM Stand 2008.

[39] Mallick PK. Composites engineering handbook. 1st editio. Dearborn, Michigan: CRC Press Taylor & Francis Group; 1997.

[40] ASTM International. Standard test methods for flexural properties of unreinforced and reinforced plastics and electrical insulating materials. D790 Annu B ASTM Stand 2002,:1–12.

[41] Yu L, Ma Y. Loading rate and temperature dependence of flexural behavior in injection-molded glass fiber reinforced polypropylene composites. Compos Part B Eng 2019;161:285–99. https://doi.org/10.1016/j.compositesb.2018.10.035.

[42] Ma Y, Ueda M, Yokozeki T, Sugahara T, Yang Y, Hamada H. A comparative study of the mechanical properties and failure behavior of carbon fiber/epoxy and carbon fiber/polyamide 6 unidirectional composites. Compos Struct 2017;160:89–99. https://doi.org/10.1016/j.compstruct.2016.10.037.

[43] López Jiménez F, Pellegrino S. Constitutive modeling of fiber composites with a soft hyperelastic matrix. Int J Solids Struct 2012;49:635–47. https://doi.org/10.1016/j.ijsolstr.2011.11.006.

[44] Beter J, Schrittesser B, Lechner B, Mansouri MR, Marano C, Fuchs PF, et al. Viscoelastic behavior of glass-fiber-reinforced silicone composites exposed to cyclic loading. Polymers (Basel) 2020;12:1–17. https://doi.org/10.3390/POLYM12091862.

[45] Bueche F. Mullins effect and rubber–filler interaction. J Appl Polym Sci 1961;5: 271–81.

[46] Beter J, Schrittesser B, Meier G, Fuchs PF, Pinter G. Influence of fiber orientation and adhesion properties on tailored fiber-reinforced elastomers. Appl Compos Mater 2020;27:149–64. https://doi.org/10.1007/s10443-020-09802-w.

[47] Zhang C, Gou X, Xiao R. Hysteresis in glass microsphere filled elastomers under cyclic loading. Polym Test 2021;95:107081. https://doi.org/10.1016/j. polymertesting.2021.107081.

[48] Beter J, Schrittesser B, Lechner B, Mansouri MR, Marano C, Fuchs PF, et al. Viscoelastic behavior of glass-fiber-reinforced silicone composites exposed to cyclic loading. Polymers (Basel) 2020;12:73–98. https://doi.org/10.1201/b11597-7.

[49] Sitiruk A, Penumadu D. Degradation in fatigue behavior of carbon fiber–vinyl ester based composites due to sea environment. Compos Part B Eng 2014;61:94–8.

[50] Gao X, Fang G, Song Y. Hysteresis loop model of unidirectional carbon fiber-reinforced ceramic matrix composites under an arbitrary cyclic load. Compos Part B Eng 2014;56:92–9.

[51] Menezes EV. Rheological properties of polymers in the linear and nonlinear viscoelastic regimes. Northwestern University; 1980.

[52] Kashyap D, Mukundan C, Kanagaraj S. Manufacturing and Characterisation of Shape-Memory Polymers and Composites. Prim. Second. Manuf. Polym. Matrix Compos.: CRC Press; 2017. p. 43–73.

[53] Zhang D, Liu L, Xu P, Zhao Y, Li Q, Lan X, et al. World's first application of a self-deployable mechanism based on shape memory polymer composites in Mars

explorations: ground-based validation and on-Mars qualification. Smart Mater Struct 2022;31:115008. https://doi.org/10.1088/1361-665X/ac93d1.

[54] Meng M, Le HR, Rizvi MJ, Grove SM. 3D FEA modelling of laminated composites in bending and their failure mechanisms. Compos Struct 2015;119:693–708. https://doi.org/10.1016/j.compstruct.2014.09.048.

[55] Liu Z, Li P, Srikanth N. Effect of delamination on the flexural response of [+45/−45/0]2s carbon fibre reinforced polymer laminates. Compos Struct 2019;209:93–102. https://doi.org/10.1016/j.compstruct.2018.10.049.

[56] CALABRO R. Mechanical characterization of elastomers under quasi-static and dynamic biaxial loading conditions. Italy, 2013.

[57] Yang Y, Fu C, Xu F. A finite strain model predicts oblique wrinkles in stretched anisotropic films. Int J Eng Sci 2020;155:103354.

[58] Mansouri MR, Fuchs PF, Criscione JC, Schrittesser B, Beter J. The contribution of mechanical interactions to the constitutive modeling of fiber-reinforced elastomers. Eur J Mech 2021;85:104081.

[59] Dieterich JH. Time-dependent friction and the mechanics of stick-slip. In: Byerlee JD, Wyss M, editors. Rock Frict. Earthq. Predict., Basel: Birkhäuser Basel; 1978, p. 790–806. https://doi.org/10.1007/978-3-0348-7182-2_15.